A hyperbolic generalized Zener model for nonlinear viscoelastic waves

Bruno Lombard, Nicolas Favrie

A hyperbolic generalized Zener model for nonlinear viscoelastic waves

N. Favrie and B. Lombard

October 19, 2022

Abstract

A macroscopic model describing nonlinear viscoelastic waves is derived in Eulerian formulation, through the introduction of relaxation tensors. It accounts for both constitutive and geometrical nonlinearities. In the case of small deformations, the governing equations recover those of the linear generalized Zener model (GZM) with memory variables, which is widely used in acoustics and seismology. The structure of the relaxation terms implies that the model is dissipative. The chosen family of specific internal energies ensures also that the model is unconditionally hyperbolic. A Godunov-type scheme with relaxation is implemented. A procedure for maintaining isochoric transformations at the discrete level is introduced. Numerical examples are proposed to illustrate the properties of viscoelastic waves and nonlinear wave phenomena.

Keywords: Hyperelasticity, generalized Zener model, memory variables, hyperbolic systems

1 Introduction

Wave motion in real media differs in many aspects from motion in an idealized elastic medium. For instance, the dispersion and attenuation induced by grain-to-grain friction can greatly affect the amplitude of the waves and their arrival times. Under the assumption of small perturbations, linear viscoelasticity is assumed to provide reasonably accurate means of describing the dissipative effects. Viscoelastic constitutive laws give the stress in terms of the past strain rate history. Among the many existing models, the linear generalized Zener model (GZM, or standard viscoelastic solid model) has proven its ability to describe the viscoelastic behaviour in small deformation of various materials [7]. It accounts for quite general attenuation laws, such as quality factors with a frequency power law. Introduction of memory variables yields a hyperbolic local-in-time evolution problem, which is computationally affordable [36, 28].

However, the linear framework is insufficient to describe wave propagation in many interesting configurations. In granular media, the physical source of the nonlinearities and attenuation is related to grain-to-grain interactions [41]. In the biomedical context, both nonlinearities and viscoelasticity are needed to model shock waves in soft solids such as the brain [13, 39, 5, 3] or the liver [8]. At a larger scale, nonlinearities and viscous damping arising during the wave propagation are commonly studied in the context of site effect assessment, and related resonance phenomena [12]. In the acoustical literature, nonlinear mechanisms are generally introduced heuristically into existing linear models. For example, a quadratic term has been added to the stress-strain relation

of the linear single body Zener model [29], but within the framework of a linear constitutive law and infinitesimal strains. The choice of a nonlinear viscoelastic model raises finally two fundamental questions: are the underlying approximations consistent? and what are the mathematical properties of the model, particularly with respect to numerical simulations?

A rational answer to these questions can be found by turning to the literature of solid mechanics. Numerous works have focused on the coupling of viscoelasticity and hyperelasticity theories in finite strain. The reader is referred to reference works such as [22, 26, 42, 35] for an overview of the dedicated literature, and to [24] for recent developments about elastomers. Since the seminal works [18, 38, 10], many studies have dealt with nonlinear viscoelastic waves, including thermodynamical analyses, traveling waves, etc. Nevertheless, these theories are often used for applications related to quasi-static configurations (i.e., where inertial effects are neglected, see e.g. [10]), even though wave propagation problems were considered recently [11, 3]. As a consequence, they often do not incorporate some particularities of wave phenomena such as a finite propagation speed, with the notable exception of [3]. This property is fundamental to get explicit-in-time numerical schemes. Finally, the model parameters should be identifiable from acoustic measurements. An interesting discussion on the acoustic identification of nonlinear parameters in polymers (PMMA) can be found in [37]. Other identification methods are based on the properties of kink waves [11, 3].

The criteria we find most important for designing a suitable model are: (i) to be thermodynamically consistent; (ii) to yield a well-posed initial-valued problem that is local in time; (iii) to degenerate towards the linear GZM in the limit-case of small deformations. An approach satisfying (i)-(ii) has been proposed in [25], in the incompressible case. The present work can be seen as an extension of this paper to the compressible case, with additionally the criterion (iii) unconditionally satisfied. On the other hand, a GZM satisfying the three criteria has already been developed by the authors, but only in the one-dimensional case [17]. The aim of this paper is to unify existing contributions and to propose a reliable model which addresses all the important features of nonlinear viscoelastic waves: finite strains in any space dimension, hyperbolicity, thermodynamical consistency, and numerics.

For this purpose, our approach is based on hyperelasticity where relaxation tensors are introduced. The model is built in an Eulerian framework and yields a nonlinear hyperbolic system of first-order partial differential equations with source terms. One parameter of the model controls the nonlinearity. On a bounded interval of values, this parameter ensures hyperbolicity of the governing equations [31, 20]. The other parameters can be calibrated in the linear regime, based on an optimization procedure described in [4]. The numerical solution can be estimated based on a splitting method: the hyperbolic part is solved by a Godunov-type HLLC scheme, while the relaxation part is solved analytically.

The paper is organised as follows. In Section 2, we present the linear GZM and the hyperelastic model in Eulerian formulation. The nonlinear GZM is introduced in Section 3, together with the equation of state and with a way to calibrate the parameters. A numerical scheme is proposed in Section 4. Numerical experiments illustrate the wave phenomena in Section 5, for various magnitudes of nonlinearity. Conclusion is drawn in Section 6.

2 Limit cases

2.1 Linear viscoelasticity

The linear GZM is largely used in acoustics and in computational seismology. This model adequately describes the usual relaxation and creep tests of solids under small deformations [7]. By optimizing its parameters, the GZM allows to finely describe dispersion relations of the waves [4]. Let us consider N mechanisms of relaxation, with relaxation frequencies θ_ℓ and positive weights $\kappa_\ell^{p,s}$ $(\ell = 1, \cdots, N)$. Then the relaxation functions of compressional (P) and shear (S) waves write respectively

$$\psi_\pi(t) = \pi_r \left(1 + \sum_{\ell=1}^{N} \kappa_\ell^p \, e^{-\theta_\ell t}\right) H(t), \qquad \psi_\mu(t) = \mu_r \left(1 + \sum_{\ell=1}^{N} \kappa_\ell^s \, e^{-\theta_\ell t}\right) H(t), \tag{1}$$

where H is the Heaviside function. Describing P and S waves with identical relaxation frequencies, as well as identical numbers of relaxation mechanisms, allows to greatly reduce the memory requirements [36]. In (1), $\pi_r = \rho_0 \, c_p^2(0)$ and $\mu_r = \rho_0 \, c_s^2(0)$ are relaxed moduli under compressional and shear loads, where $c_p(0)$ and $c_s(0)$ denote the phase velocities of P and S waves at zero frequency, respectively, and ρ_0 is a reference density. The unrelaxed moduli are

$$\pi_u = \pi_r \left(1 + \sum_{\ell=1}^{N} \kappa_\ell^p\right) = \rho_0 \, c_p^2(\infty), \qquad \mu_u = \mu_r \left(1 + \sum_{\ell=1}^{N} \kappa_\ell^s\right) = \rho_0 \, c_s^2(\infty), \tag{2}$$

where $c_p(\infty)$ and $c_s(\infty)$ are the phase velocities of P and S waves at infinite frequency. Additional details may be found in [28].

A naive use of the relaxation functions (1) would involve convolution products, which is computationally too expensive. Introducing the so-called *memory variables* $\boldsymbol{\xi}_\ell$ provides a local-in-time hyperbolic system with source term. The velocity-stress formulation writes [28]:

$$\begin{cases} \rho_0 \dfrac{\partial \boldsymbol{v}}{\partial t} = \operatorname{div} \boldsymbol{\sigma}, & \text{(3a)} \\ \dfrac{\partial \boldsymbol{\sigma}}{\partial t} = (\pi_u - 2\,\mu_u) \operatorname{div} \boldsymbol{v}\, \boldsymbol{I} + 2\,\mu_u \boldsymbol{D} + \displaystyle\sum_{\ell=1}^{N} \boldsymbol{\xi}_\ell, & \text{(3b)} \\ \dfrac{\partial \boldsymbol{\xi}_\ell}{\partial t} = -\theta_\ell \left((\pi_r \kappa_\ell^p - 2\mu_r \kappa_\ell^s) \operatorname{div} \boldsymbol{v}\, \boldsymbol{I} + 2\mu_r \kappa_\ell^s \, \boldsymbol{D} + \boldsymbol{\xi}_\ell \right), \qquad \ell = 1, \cdots, N, & \text{(3c)} \end{cases}$$

where $\boldsymbol{v} = (u, v, w)^T$ is the velocity, $\boldsymbol{\sigma}$ is the Cauchy stress, $\boldsymbol{\xi}_\ell$ are symmetric tensors, $\boldsymbol{I}$ is the identity tensor, and $\boldsymbol{D} = \operatorname{sym}(\mathbf{grad}\, \boldsymbol{v})$ is the rate of deformation tensor.

2.2 Nonlinear hyperelasticity

The differential operators are applied in the Eulerian coordinates $\boldsymbol{x} = (x, y, z)^\top \in \mathbb{R}^3$. The deformation gradient is $\boldsymbol{F} = \partial \boldsymbol{x} / \partial \boldsymbol{X}$, were $\boldsymbol{X}$ are the Lagrangian coordinates. The velocity is $\boldsymbol{v} = d\boldsymbol{x}/dt$, where d/dt is the time derivative at constant particle $\boldsymbol{X}$. The conservation of mass, momentum and energy in Eulerian formulation writes:

$$\begin{cases} \dfrac{\partial \rho}{\partial t} + \operatorname{div}(\rho \boldsymbol{v}) = 0, & \text{(4a)} \\ \dfrac{\partial (\rho \boldsymbol{v})}{\partial t} + \operatorname{div}(\rho \boldsymbol{v} \otimes \boldsymbol{v} - \boldsymbol{\sigma}) = \boldsymbol{0}, & \text{(4b)} \\ \dfrac{\partial (\rho E)}{\partial t} + \operatorname{div}(\rho \boldsymbol{v} E - \boldsymbol{\sigma}.\boldsymbol{v}) = 0. & \text{(4c)} \end{cases}$$

Time differentiation of $\boldsymbol{F}.\boldsymbol{F}^{-1}$ and use of $d\boldsymbol{F}/dt = \mathbf{grad}\boldsymbol{v}.\,\boldsymbol{F}$ yields the kinematic equation

$$\frac{d}{dt}\boldsymbol{F}^{-\top} = -\mathbf{grad}^{\top}\boldsymbol{v}.\,\boldsymbol{F}^{-\top}. \tag{5}$$

This writing is not usual in solid mechanics. However, it is well adapted to the Eulerian formulation followed in this article. The density is $\rho = \rho_0/|\boldsymbol{F}|$, where ρ_0 is a reference density and $|\bullet| = \det(\bullet)$. The total specific energy E is

$$E = \frac{\boldsymbol{v}^2}{2} + e(\eta, \boldsymbol{C}^{-1}), \tag{6}$$

where e is the specific internal energy, η is the specific entropy, and $\boldsymbol{C} = \boldsymbol{F}^T.\boldsymbol{F}$ is the right Cauchy-Green strain tensor. The nullity of dissipation yields the Cauchy stress tensor:

$$\boldsymbol{\sigma} = -2\,\rho\,\boldsymbol{F}^{-\top}.\frac{\partial e}{\partial \boldsymbol{C}^{-1}}.\boldsymbol{F}^{-1}. \tag{7}$$

Using $\boldsymbol{C}^{-1}$ in (6) ensures material frame-indifference, see Section 5.4 of [22]. The system (4)-(5) yields 7 waves [21]. One of these wave is linearly degenerate, the other are nonlinear and may have a complex structure (genuinely or non genuinely nonlinear waves). The reader is refered to [33, 23] for a complete study in a particular case.

3 Nonlinear GZM

3.1 Objective

We aim to build a model that satisfies the following properties:

(i) recovering the linear GZM (3) in the case of infinitesimal deformation;

(ii) recovering the hyperelastic model (4) in the lossless case;

(iii) satisfying the second principle of thermodynamics;

(iv) being unconditionally hyperbolic.

This new model is built by adding relaxation terms to the system (4), as shown in Section 3.2. The study of this model in small deformations in Section 3.3 leads, by identifying the parameters, to the linear GZM (criterion (i)). When these terms cancel, the hyperelastic model is recovered, so that criterion (ii) is satisfied. The general form of the relaxation terms is determined by imposing a positive dissipation, thus satisfying criterion (iii). Finally, criterion (iv) is satisfied by choosing particular forms of specific internal energy (Section 3.4).

3.2 Governing equations

Kinematic equations. The conservation equations (4) are unchanged. However, we introduce new kinematic variables denoted $\boldsymbol{F}_\ell$. In a rheological diagram, $\boldsymbol{F}_0$ corresponds to the true deformation gradient tensor. Instead of (5), the kinematic equations are now:

$$\begin{cases} \dfrac{d}{dt}\boldsymbol{F}_0^{-\top} = -\mathbf{grad}^{\top}\boldsymbol{v}.\,\boldsymbol{F}_0^{-\top}, & \text{(8a)} \\ \dfrac{d}{dt}\boldsymbol{F}_\ell^{-\top} = -\mathbf{grad}^{\top}\boldsymbol{v}.\,\boldsymbol{F}_\ell^{-\top} + \boldsymbol{R}_\ell.\,\boldsymbol{F}_\ell^{-\top}, \qquad \ell = 1, \cdots, N, & \text{(8b)} \end{cases}$$

where $\boldsymbol{R}_\ell$ are symmetric second-order tensors. These relaxation terms will be determined later. A similar approach is used to model viscoplasticity in [14] or incompressible viscoelasticity in [25]. Equation (8a) describes the equilibrium elastic part of the behaviour. It can be merged with (8b) by setting $\boldsymbol{R}_0 = \boldsymbol{0}$, as done from now. Based on (8b), the time derivative of $\boldsymbol{C}_\ell^{-1} = \boldsymbol{F}_\ell^{-1}.\boldsymbol{F}_\ell^{-\top}$ writes:

$$\frac{d}{dt}\boldsymbol{C}_\ell^{-1} = -2\,\boldsymbol{F}_\ell^{-1}.(\boldsymbol{D} - \boldsymbol{R}_\ell).\boldsymbol{F}_\ell^{-\top}, \qquad \ell = 1, \cdots, N. \tag{9}$$

For further calibration of the equation of state and numerical resolution of the governing equations, the time derivative of $J_\ell = |\boldsymbol{C}_\ell| = |\boldsymbol{F}_\ell|^2$ is needed. This notation should not be confused with the standard notation $\mathcal{J}_\ell = |\boldsymbol{F}_\ell|$, hence $J_\ell = \mathcal{J}_\ell^2$. Based on (9), it follows that:

$$\frac{d}{dt}J_\ell = 2J_\ell\,(\mathrm{div}\boldsymbol{v} - \mathrm{tr}\boldsymbol{R}_\ell), \qquad \ell = 1, \cdots, N. \tag{10}$$

Using (10) and $J_\ell^{-1} = (J_\ell^{-1/2})^2$, one obtains

$$\frac{d}{dt}J_\ell^{-1/2} + J_\ell^{-1/2}\mathrm{div}\boldsymbol{v} = J_\ell^{-1/2}\mathrm{tr}\boldsymbol{R}_\ell, \qquad \ell = 1, \cdots, N. \tag{11}$$

Dissipation of energy. The total specific energy is

$$E = \frac{\boldsymbol{v}^2}{2} + \sum_{\ell=0}^{N} e_\ell\left(\eta, \boldsymbol{C}_\ell^{-1}\right), \tag{12}$$

where the internal energy $e = \sum_\ell e_\ell$ satisfies the differential equation $\rho\, de/dt = \boldsymbol{\sigma} : \boldsymbol{D}$, consistently with the conservation laws (4). The Cauchy stress

$$\boldsymbol{\sigma} = \sum_{\ell=0}^{N} \boldsymbol{\sigma}_\ell \tag{13}$$

is deduced from the Gibbs identity for de/dt, and from the second principle of thermodynamics. For this purpose, one introduces the dissipation $\mathcal{D} = \rho T\, d\eta/dt \geq 0$, where $T = \partial E/\partial\eta \geq 0$ is the temperature, and η is the entropy. Using (9), (12), (13) and the symmetry of $\boldsymbol{D}$ and $\boldsymbol{R}_\ell$, the dissipation $\mathcal{D}$ writes

$$\begin{aligned}
\mathcal{D} &= \sum_{\ell=0}^{N}\left(\boldsymbol{\sigma}_\ell : \boldsymbol{D} - \rho\frac{\partial e_\ell}{\partial \boldsymbol{C}_\ell^{-1}} : \frac{d}{dt}\boldsymbol{C}_\ell^{-1}\right), \\
&= \sum_{\ell=0}^{N}\left(\boldsymbol{\sigma}_\ell : \boldsymbol{D} - \rho\frac{\partial e_\ell}{\partial \boldsymbol{C}_\ell^{-1}} : \left(-2\,\boldsymbol{F}_\ell^{-1}.(\boldsymbol{D} - \boldsymbol{R}_\ell).\boldsymbol{F}_\ell^{-\top}\right)\right), \\
&= \sum_{\ell=0}^{N}\left(\left(\boldsymbol{\sigma}_\ell + 2\,\rho\,\boldsymbol{F}_\ell^{-\top}.\frac{\partial e_\ell}{\partial \boldsymbol{C}_\ell^{-1}}.\boldsymbol{F}_\ell^{-1}\right) : \boldsymbol{D} - 2\,\rho\,\boldsymbol{F}_\ell^{-\top}.\frac{\partial e_\ell}{\partial \boldsymbol{C}_\ell^{-1}}.\boldsymbol{F}_\ell^{-1} : \boldsymbol{R}_\ell\right), \\
&\geq 0.
\end{aligned} \tag{14}$$

This inequality is satisfied whatever $\boldsymbol{D}$, which implies

$$\boldsymbol{\sigma}_\ell = -2\,\rho\,\boldsymbol{F}_\ell^{-\top}.\frac{\partial e_\ell}{\partial \boldsymbol{C}_\ell^{-1}}.\boldsymbol{F}_\ell^{-1}, \qquad \ell = 0, \cdots, N, \tag{15}$$

and

$$\sum_{\ell=0}^{N}\boldsymbol{\sigma}_\ell : \boldsymbol{R}_\ell = \sum_{\ell=0}^{N}\mathrm{tr}\left(\boldsymbol{\sigma}_\ell.\boldsymbol{R}_\ell\right) \geq 0. \tag{16}$$

Property 1 *A sufficient condition to ensure* (16) *is to choose:*

$$\boldsymbol{R}_\ell = \alpha_\ell\, \boldsymbol{\sigma}_\ell + \beta_\ell\, tr\boldsymbol{\sigma}_\ell\, \boldsymbol{I}, \qquad \ell = 1, \cdots, N, \tag{17}$$

with $\alpha_\ell \geq 0$ *and* $\beta_\ell \geq -\alpha_\ell/3$.

The parameters α_ℓ and β_ℓ are scalars and they may depend on any parameters such as temperature, invariant of the stress, pressure, etc. In the following and for the sake of simplicity, we will consider them as constant.

Proof. The tensor $\boldsymbol{\sigma}_\ell$ is split into its spheric and deviatoric parts:

$$\boldsymbol{\sigma}_\ell = -p_\ell\, \boldsymbol{I} + \boldsymbol{S}_\ell, \text{ with } \mathrm{tr}\boldsymbol{S}_\ell = 0. \tag{18}$$

Then one has:

$$\begin{aligned} \mathrm{tr}\left(\boldsymbol{\sigma}_\ell.\, \boldsymbol{R}_\ell\right) &= \mathrm{tr}\left(\left(-p_\ell\, \boldsymbol{I} + \boldsymbol{S}_\ell\right)\left(\alpha_\ell(-p_\ell\, \boldsymbol{I} + \boldsymbol{S}_\ell) + \beta_\ell(-3\, p_\ell)\, \boldsymbol{I}\right)\right), \\ &= \left(\alpha_\ell + 3\,\beta_\ell\right)\, p_\ell^2\, \mathrm{tr}\boldsymbol{I} - \left(2\,\alpha_\ell + 3\,\beta_\ell\right)\, p_\ell\, \mathrm{tr}\boldsymbol{S}_\ell + \alpha_\ell\, \mathrm{tr}\boldsymbol{S}_\ell^2, \\ &= 3\left(\alpha_\ell + 3\,\beta_\ell\right)\, p_\ell^2 + \alpha_\ell\, \boldsymbol{S}_\ell : \boldsymbol{S}_\ell, \\ &\geq 0, \end{aligned} \tag{19}$$

which concludes the proof. ■

Property 1 generalizes the analysis performed in [14] in the case of viscoplasticity. The determination of α_ℓ and β_ℓ will be discussed in Section 3.3 to ensure that, in the limit of small deformation, one recovers the linear GZM used in acoustics. From now on, we focus our study on the isotropic case for which one knows an equation of state (EOS) that guarantees the hyperbolicity of the model. Nevertheless, extension to anisotropic models could be considered without major modifications (in principle).

3.3 Small deformations

In the case of small deformations, the Lagrangian and Eulerian descriptions are identical and $\boldsymbol{C}_\ell^{-1} \approx \boldsymbol{I} - 2\,\boldsymbol{\varepsilon}_\ell$, where $\boldsymbol{\varepsilon}_\ell$ are second-order symmetric tensors. Using (9) leads to

$$\frac{\partial \boldsymbol{\varepsilon}_\ell}{\partial t} = \boldsymbol{D} - \boldsymbol{R}_\ell, \qquad \ell = 1, \cdots, N. \tag{20}$$

The constitutive laws for linear isotropic solids write $\boldsymbol{\sigma}_\ell = \lambda_\ell\, \mathrm{tr}\boldsymbol{\varepsilon}_\ell\, \boldsymbol{I} + 2\,\mu_\ell\, \boldsymbol{\varepsilon}_\ell$, where λ_ℓ and μ_ℓ are Lamé coefficients, to be determined. Time differentiating the constitutive laws and using (20) gives

$$\frac{\partial \boldsymbol{\sigma}_\ell}{\partial t} = \lambda_\ell\, \mathrm{div}\boldsymbol{v}\, \boldsymbol{I} + 2\,\mu_\ell\, \boldsymbol{D} + \boldsymbol{\xi}_\ell, \qquad \ell = 1, \cdots, N, \tag{21}$$

where the second-order symmetric tensors $\boldsymbol{\xi}_\ell$ write

$$\boldsymbol{\xi}_\ell = -\left(\lambda_\ell\, \mathrm{tr}\boldsymbol{R}_\ell\, \boldsymbol{I} + 2\,\mu_\ell\, \boldsymbol{R}_\ell\right), \qquad \ell = 1, \cdots, N, \tag{22}$$

and $\boldsymbol{\xi}_0 = \boldsymbol{0}$. Introducing the unrelaxed moduli

$$\pi_u = \sum_{\ell=0}^{N} \left(\lambda_\ell + 2\,\mu_\ell\right), \qquad \mu_u = \sum_{\ell=0}^{N} \mu_\ell, \tag{23}$$

and summing (21) over ℓ, one obtains

$$\frac{\partial \boldsymbol{\sigma}}{\partial t} = (\pi_u - 2\,\mu_u)\,\mathrm{div}\boldsymbol{v}\,\boldsymbol{I} + 2\,\mu_u \boldsymbol{D} + \sum_{\ell=1}^{N} \boldsymbol{\xi}_\ell, \tag{24}$$

which recovers the evolution of $\boldsymbol{\sigma}$ in the linear GZM (3b). It remains to determine the time evolution of $\boldsymbol{\xi}_\ell$. From (21), it follows

$$\frac{\partial}{\partial t}\mathrm{tr}\boldsymbol{\sigma}_\ell = (3\lambda_\ell + 2\mu_\ell)\ \mathrm{div}\boldsymbol{v} + \mathrm{tr}\boldsymbol{\xi}_\ell, \qquad \ell = 1, \cdots, N. \tag{25}$$

Equations (17) and (22) yield

$$\boldsymbol{\xi}_\ell = -\left(A_\ell\,\boldsymbol{\sigma}_\ell + B_\ell\,\mathrm{tr}\boldsymbol{\sigma}_\ell\,\boldsymbol{I}\right), \qquad \ell = 1, \cdots, N, \tag{26}$$

with

$$A_\ell = 2\,\mu_\ell\,\alpha_\ell, \qquad B_\ell = \lambda_\ell\,\alpha_\ell + (3\lambda_\ell + 2\,\mu_\ell)\ \beta_\ell, \qquad \ell = 1, \cdots, N. \tag{27}$$

From (21), (25) and (26), one deduces

$$\frac{\partial \boldsymbol{\xi}_\ell}{\partial t} = -A_\ell\,(\lambda_\ell\,\mathrm{div}\boldsymbol{v}\,\boldsymbol{I} + 2\,\mu_\ell\,\boldsymbol{D} + \boldsymbol{\xi}_\ell) - B_\ell\,((3\lambda_\ell + 2\mu_\ell)\ \mathrm{div}\boldsymbol{v} + \mathrm{tr}\boldsymbol{\xi}_\ell)\ \boldsymbol{I}, \qquad \ell = 1, \cdots, N. \tag{28}$$

Identification with (3c), where no term $\mathrm{tr}\boldsymbol{\xi}_\ell$ occurs, implies $B_\ell = 0$, and (27) gives

$$\beta_\ell = -\frac{\lambda_\ell}{3\lambda_\ell + 2\mu_\ell}\,\alpha_\ell, \qquad \ell = 1, \cdots, N. \tag{29}$$

The equation (28) then recovers the evolution of $\boldsymbol{\xi}_\ell$ in the linear GZM (3c) if the following conditions are satisfied ($\ell = 1, \cdots, N$):

$$\lambda_\ell = \pi_r \kappa_\ell^p - 2\mu_r \kappa_\ell^s, \qquad \mu_\ell = \mu_r \kappa_\ell^s, \qquad \alpha_\ell = \frac{\theta_\ell}{2\mu_\ell} = \frac{\theta_\ell}{2\mu_r \kappa_\ell^s}. \tag{30}$$

The positive parameters of the linear GZM κ_ℓ^p, κ_ℓ^s and θ_ℓ can be obtained from the attenuation of linear P and S waves [4]. The elastic moduli λ_0 and μ_0 are determined by using (23):

$$\lambda_0 = \pi_u - 2\mu_u - \sum_{\ell=1}^{N} \lambda_\ell, \qquad \mu_0 = \mu_u - \sum_{\ell=1}^{N} \mu_\ell. \tag{31}$$

One notices that α_ℓ in (30) and β_ℓ in (29) naturally satisfy the sign requirements of Property 1.

3.4 Equations of state

Materials with a specific internal energy (12) in separable form are considered:

$$e_\ell(\eta, \boldsymbol{C}_\ell^{-1}) = e_{h\ell}(J_\ell) + e_{s\ell}\left(\hat{\boldsymbol{C}}_\ell^{-1}\right), \qquad \ell = 1, \cdots, N, \tag{32}$$

with the unimodular tensor $\hat{\boldsymbol{C}}_\ell^{-1} = \boldsymbol{C}_\ell^{-1}/\left|\boldsymbol{C}_\ell^{-1}\right|^{1/3}$. One introduces the unimodular parts of the Finger tensors $\hat{\boldsymbol{G}}_\ell = \boldsymbol{G}_\ell/\left|\boldsymbol{G}_\ell\right|^{1/3}$, where $\boldsymbol{G}_\ell = \boldsymbol{B}_\ell^{-1}$ is the Finger tensor and $\boldsymbol{B}_\ell = \boldsymbol{F}_\ell.\boldsymbol{F}_\ell^T$ is the left Cauchy-Green deformation tensor. For isotropic solids, $e_{s\ell}$ can be written as a function of only two invariants of $\hat{\boldsymbol{C}}_\ell^{-1}$:

$$e_{s\ell}(\hat{\boldsymbol{C}}_\ell^{-1}) = e_{s\ell}(j_{1\ell}, j_{2\ell}), \qquad j_{k\ell} = \mathrm{tr}\left(\hat{\boldsymbol{C}}_\ell^{-1}\right)^k \equiv \mathrm{tr}\left(\hat{\boldsymbol{G}}_\ell\right)^k. \tag{33}$$

Based on the usual relations of tensorial calculus

$$\frac{\partial}{\partial \boldsymbol{A}} \mathrm{tr}\left(\boldsymbol{A}^n\right) = n\left(\boldsymbol{A}^T\right)^{n-1}, \qquad \frac{\partial}{\partial \boldsymbol{A}} \det(\boldsymbol{A}) = \det(\boldsymbol{A})\, \boldsymbol{A}^{-\top}, \tag{34}$$

the Cauchy stress in (15) writes ($\ell = 1, \cdots, N$):

$$\begin{aligned} \boldsymbol{\sigma}_\ell &= -2\,\rho\, \boldsymbol{F}_\ell^{-\top} \left(\frac{\partial e_{h\ell}}{\partial J_\ell} \frac{\partial J_\ell}{\partial \boldsymbol{C}_\ell^{-1}} + \sum_{k=1}^{2} \frac{\partial e_{s\ell}}{\partial j_{k\ell}} \frac{\partial j_{k\ell}}{\partial \boldsymbol{C}_\ell^{-1}} \right) . \boldsymbol{F}_\ell^{-1}, \\ &= -2\,\rho\, \boldsymbol{F}_\ell^{-\top} \left(-\frac{\partial e_{h\ell}}{\partial J_\ell}\, J_\ell\, \boldsymbol{C}_\ell + \sum_{k=1}^{2} \frac{\partial e_{s\ell}}{\partial j_{k\ell}}\, k \left(J_\ell^{k/3} \left(\boldsymbol{C}_\ell^{-1}\right)^k - \frac{j_{k\ell}}{3}\, \boldsymbol{I} \right) \boldsymbol{C}_\ell \right) . \boldsymbol{F}_\ell^{-1}, \\ &\equiv -p_\ell\, \boldsymbol{I} + \boldsymbol{S}_\ell, \end{aligned} \tag{35}$$

with $\mathrm{tr}\boldsymbol{S}_\ell = 0$. The hydrodynamic part of the stress is thus

$$p_\ell = -2\rho \frac{\partial e_{h\ell}}{\partial J_\ell}\, J_\ell, \tag{36}$$

whereas the deviatoric part of the stress writes

$$\begin{aligned} \boldsymbol{S}_\ell &= -2\rho \left(\frac{\partial e_{s\ell}}{\partial j_{1\ell}} \left(J_\ell^{1/3} \boldsymbol{F}_\ell^{-\top} . \boldsymbol{F}_\ell^{-1} - \frac{j_{1\ell}}{3}\, \boldsymbol{I} \right) + 2 \frac{\partial e_{s\ell}}{\partial j_{2\ell}} \left(J_\ell^{2/3} \left(\boldsymbol{F}_\ell^{-\top} . \boldsymbol{F}_\ell^{-1} \right)^2 - \frac{j_{2\ell}}{3}\, \boldsymbol{I} \right) \right), \\ &= -2\rho \left(\frac{\partial e_{s\ell}}{\partial j_{1\ell}} \left(\hat{\boldsymbol{G}}_\ell - \frac{j_{1\ell}}{3}\, \boldsymbol{I} \right) + 2 \frac{\partial e_{s\ell}}{\partial j_{2\ell}} \left(\left(\hat{\boldsymbol{G}}_\ell \right)^2 - \frac{j_{2\ell}}{3}\, \boldsymbol{I} \right) \right). \end{aligned} \tag{37}$$

The last expression in (37) recovers the shear tensor given in [16, 20]: in the isotropic case, the stress equations deduced from the Finger tensors and from $\boldsymbol{C}_\ell^{-1}$ are thus the same. Now we determine the stresses induced by the internal energy (32).

Hydrodynamic stress. The hydrodynamic part of the energy is chosen in the form:

$$e_{h\ell}(\eta, J_\ell) = \frac{d_\ell}{\rho_0} \left(J_\ell^{1/2} - 1 \right)^2, \qquad \ell = 0, \cdots, N, \tag{38}$$

where ρ_0 is a reference density. In the hyperelastic case ($N = 0$), the convexity of (38), combined with criteria on the shear part of the energy precised further, is a sufficent condition to ensure the hyperbolicity of the model [31]. The proof made in [31] generalizes directly to the case of $N \geq 1$ relaxation mechanisms. Using (36) and $\rho = \rho_0 / J_0^{1/2}$ yields the pressures

$$p_\ell = 2\, d_\ell \frac{\rho}{\rho_0} J_\ell^{1/2} \left(1 - J_\ell^{1/2} \right) = 2\, d_\ell \left(\frac{J_\ell}{J_0} \right)^{1/2} \left(1 - J_\ell^{1/2} \right), \qquad \ell = 0, \cdots, N. \tag{39}$$

The parameter d_ℓ is determined in two steps, based on the limit-case of small deformations. First, in the isentropic case, the differential of $p_\ell(\eta, \rho, J_\ell)$ writes

$$\frac{dp_\ell}{dt} = \frac{dp_\ell}{d\rho} \frac{d\rho}{dt} + \frac{dp_\ell}{dJ_\ell} \frac{dJ_\ell}{dt}. \tag{40}$$

The latter is deployed based on (36), on the conservation of mass (4a) and on the transport of J_ℓ (10), leading to

$$\frac{dp_\ell}{dt} = -2\rho\, J_\ell \left(\frac{\partial e_{h\ell}}{\partial J_\ell} + 2 J_\ell \frac{\partial^2 e_{h\ell}}{\partial J_\ell^2} \right) \mathrm{div}\boldsymbol{v} + 4\rho\, J_\ell \left(\frac{\partial e_\ell^h}{\partial J_\ell} + 2 J_\ell \frac{\partial^2 e_{h\ell}}{\partial J_\ell^2} \right) \mathrm{tr}\boldsymbol{R}_\ell. \tag{41}$$

Second, the decomposition (18) leads to $p_\ell = -1/3\,\mathrm{tr}\boldsymbol{\sigma}_\ell$, which is then time differentiated in the case of small deformations (25):

$$\frac{dp_\ell}{dt} \approx \frac{\partial p_\ell}{\partial t} = -\left(\lambda_\ell + \frac{2}{3}\mu_\ell\right) \mathrm{div}\boldsymbol{v} - \frac{1}{3}\mathrm{tr}\boldsymbol{\xi}_\ell. \tag{42}$$

Identification between (41) and (42) gives

$$2\rho\, J_\ell \left(\frac{\partial e_{h\ell}}{\partial J_\ell} + 2\, J_\ell \frac{\partial^2 e_{h\ell}}{\partial J_\ell^2}\right) = \lambda_\ell + \frac{2}{3}\mu_\ell. \tag{43}$$

The left hand side of (43) is deduced from the hydrodynamic energy (38) and equals $2(\rho/\rho_0)J_\ell\, d_\ell$. For small deformations, $\rho \approx \rho_0$ and $J_\ell \approx 1$. Using (43) yields the parameter

$$d_\ell = \frac{1}{2}\left(\lambda_\ell + \frac{2}{3}\mu_\ell\right), \qquad \ell = 0, \cdots, N. \tag{44}$$

Additionally, the term before $\mathrm{div}\boldsymbol{v}$ in (41) is a bulk modulus $K_{h\ell} = \rho\, c_{h\ell}^2$, where $c_{h\ell}$ is an hydrodynamic sound speed. It follows ($\ell = 0, \cdots, N$):

$$\begin{aligned} c_{h\ell}^2 &= 2\, J_\ell \left(\frac{\partial e_{h\ell}}{\partial J_\ell} + 2J_\ell \frac{\partial^2 e_{h\ell}}{\partial J_\ell^2}\right) = \frac{2d_\ell}{\rho_0} J_\ell, \\ &= \frac{1}{\rho_0}\left(\lambda_\ell + \frac{2}{3}\mu_\ell\right) J_\ell. \end{aligned} \tag{45}$$

Hydrodynamic sound speeds are not wave velocities deduced from a Riemann problem, which is why they do not involve the elastic moduli $\lambda_\ell + 2\mu_\ell$ of plane compression waves. Lastly, it is emphasized that the inequality $J_\ell > 0$ must always be satisfied to yield real hydrodynamic sound speeds.

Deviatoric stress. The shear part of the energy (33) is chosen in the form [16]:

$$e_{s\ell}(j_{1\ell}, j_{2\ell}) = \frac{\mu_\ell}{4\rho_0}\left(\chi_\ell\, j_{2\ell} + \frac{1-2\chi_\ell}{3}\, j_{1\ell}^2 + 3\,(\chi_\ell - 1)\right), \qquad \ell = 0, \cdots, N. \tag{46}$$

Here χ_ℓ can be viewed as new nonlinear parameters. For small deformations and any χ_ℓ, the Hooke law is recovered. Thus, these parameters are important only in the case of large shear deformations. They can be used to fit experimental data. The deviatoric part of the stress is finally deduced from (37) and (46), through

$$\frac{\partial e_{s\ell}}{\partial j_{1\ell}} = \frac{\mu_\ell}{6\,\rho_0}\,(1-2\chi_\ell)\, j_{1\ell}, \qquad \frac{\partial e_{s\ell}}{\partial j_{2\ell}} = \frac{\mu_\ell}{4\,\rho_0}\chi_\ell, \qquad \ell = 0, \cdots, N. \tag{47}$$

A theoretical analysis of (46) has been performed in hyperelasticity [20], where the hyperbolicity was proven under the sufficient condition $-1 \leq \chi \leq 0.5$. Following [31], one can extend this property to the viscoelastic case.

Property 2 *The viscoelastic model with stress* (35)*, hydrodynamic energy* (38) *and shear energy* (46)*, is hyperbolic under the sufficient condition:*

$$-1 \leq \chi_\ell \leq 0.5, \qquad \ell = 1, \cdots, N. \tag{48}$$

The limit case $\chi_\ell = -1$ corresponds to Neo-Hookean solids. Other choices of EOS are of course possible, for example the Mooney-Rivlin model often used to describe elastomers, or the Murnaghan model widely used for non-destructive testing of geomaterials [2]. However, hyperbolicity has not been proven for these models.

3.5 Final system

We collect here the governing equations of the generalized nonlinear Zener model. Their numerical discretization will be detailed in Section 4. The conservation laws are

$$\begin{cases} \dfrac{\partial \rho}{\partial t} + \operatorname{div}(\rho \boldsymbol{v}) = 0, & \text{(49a)} \\ \dfrac{\partial (\rho \boldsymbol{v})}{\partial t} + \operatorname{div}(\rho \boldsymbol{v} \otimes \boldsymbol{v} - \boldsymbol{\sigma}) = \boldsymbol{s}, & \text{(49b)} \end{cases}$$

where $\boldsymbol{s}$ is a bulk force term. The conservation of energy (4c) is not required, since the internal energy does not depend explicitly on the entropy. The components of the Cauchy stress $\boldsymbol{\sigma}$ (13)-(35) are the hydrodynamic pressure p_ℓ (39) and the shear stress $\boldsymbol{S}_\ell$ (37)-(46).

We introduce the covectors $\boldsymbol{e}_\ell^\beta$ as the columns of $\boldsymbol{F}_\ell^{-\top} = (\boldsymbol{e}_\ell^1, \boldsymbol{e}_\ell^2, \boldsymbol{e}_\ell^3)$, with $\boldsymbol{e}_\ell^\beta = (a_\ell^\beta, b_\ell^\beta, c_\ell^\beta)^\top$. Defining $\boldsymbol{a}_\ell = (a_\ell^1, a_\ell^2, a_\ell^3)^\top$, $\boldsymbol{b}_\ell = (b_\ell^1, b_\ell^2, b_\ell^3)^\top$, $\boldsymbol{c}_\ell = (c_\ell^1, c_\ell^2, c_\ell^3)^\top$, then the unimodular Finger tensors in (37) write:

$$\hat{\boldsymbol{G}}_\ell = \frac{1}{|\boldsymbol{G}_\ell|^{1/3}} \begin{pmatrix} \boldsymbol{a}_\ell.\boldsymbol{a}_\ell & \boldsymbol{a}_\ell.\boldsymbol{b}_\ell & \boldsymbol{a}_\ell.\boldsymbol{c}_\ell \\ \boldsymbol{a}_\ell.\boldsymbol{b}_\ell & \boldsymbol{b}_\ell.\boldsymbol{b}_\ell & \boldsymbol{b}_\ell.\boldsymbol{c}_\ell \\ \boldsymbol{a}_\ell.\boldsymbol{c}_\ell & \boldsymbol{b}_\ell.\boldsymbol{c}_\ell & \boldsymbol{c}_\ell.\boldsymbol{c}_\ell \end{pmatrix}, \qquad \ell = 0, \cdots, N. \tag{50}$$

The kinematic equations write then

$$\begin{cases} \dfrac{\partial \boldsymbol{e}_\ell^\beta}{\partial t} + \mathbf{grad}\, \boldsymbol{e}_\ell^\beta.\boldsymbol{v} + \boldsymbol{e}_\ell^\beta.\, \mathbf{grad}\, \boldsymbol{v} = \boldsymbol{R}_\ell.\, \boldsymbol{e}_\ell^\beta, & \ell = 0, \cdots, N, \quad \beta = 1, 2, 3, & \text{(51a)} \\ \dfrac{\partial}{\partial t} J_\ell^{-1/2} + \operatorname{div}\left(J_\ell^{-1/2}\, \boldsymbol{v} \right) = \phi_\ell, & \ell = 0, \cdots, N. & \text{(51b)} \end{cases}$$

In the right hand side of (51a), the relaxation tensors are deduced from (17), (29) and (30):

$$\boldsymbol{R}_0 = \boldsymbol{0}, \qquad \boldsymbol{R}_\ell = \frac{\theta_\ell}{2\mu_\ell} \left(\boldsymbol{\sigma}_\ell - \frac{\lambda_\ell}{3\lambda_\ell + 2\mu_\ell} \operatorname{tr}\boldsymbol{\sigma}_\ell\, \boldsymbol{I} \right), \qquad \ell = 1, \cdots, N. \tag{52}$$

The equation (51b) is redundant with (51a). However, this additional equation is useful from a numerical point of view, for two reasons: (i) it enforces isochoric transformations to remain isochoric at the discrete level; (ii) it enforces $J_\ell > 0$, as required by the hydrodynamic sound speeds in (45). Justification of (i) is given in Appendix A. Based on (11) and on (52), the scalars $\phi_\ell = J_\ell^{-1/2} \operatorname{tr}\boldsymbol{R}_\ell$ in (51b) are:

$$\phi_0 = 0, \qquad \phi_\ell = J_\ell^{-1/2} \frac{\theta_\ell}{3\lambda_\ell + 2\mu_\ell} \operatorname{tr}\boldsymbol{\sigma}_\ell, \qquad \ell = 1, \cdots, N. \tag{53}$$

The systems (49) and (51) involve $14 + 10 \times N$ partial differential equations. They need to be completed by initial conditions. In the case of forcing by a source point $\boldsymbol{s} \neq \boldsymbol{0}$, then the initial data are $\rho(\bullet, t = 0) = \rho_0$, $\boldsymbol{v}(\bullet, t = 0) = \boldsymbol{0}$, $\boldsymbol{F}_\ell^{-\top}(\bullet, t = 0) = \boldsymbol{I}$ and $J_\ell^{-1/2}(\bullet, t = 0) = 1$.

Calibration. The parameters of the nonlinear GZM are determined as follows:

1. the attenuation of the P- and S-wave is assumed to be known, for example via the quality factors of the compressional waves Q_p and of the shear waves Q_s. The reader is referred to [7] for a precise definition of these quantities describing the attenuation. An optimization procedure on the quality factors then provides the relaxation frequencies θ_ℓ and the weights $\kappa_\ell^{p,s}$;

2. the phase velocities of the compressional waves $c_p(0)$ and of the shear waves $c_s(0)$ provide the relaxed moduli π_r and μ_r, and then the unrelaxed moduli π_u and μ_u (23);

3. the Lamé coefficients (30)-(31) are deduced, and then the parameters d_ℓ (44) involved in the hydrodynamic pressure;

4. the only free parameters are the χ_ℓ involved in the shear stress (46), with $-1 \leq \chi_\ell \leq 0.5$ to guarantee the hyperbolicity.

In the case of null dissipation, the weights are $\kappa_\ell^p = \kappa_\ell^s \equiv 0$ for $\ell = 1, \cdots, N$. It follows $\pi_u = \pi_r$, $\mu_u = \mu_r$ (23), $\lambda_\ell = \mu_\ell \equiv 0$ for $\ell = 1, \cdots, N$ (30), and $\lambda_0 = \pi_r$, $\mu_0 = \mu_r$ (31). One has $\boldsymbol{\sigma}_\ell = \mathbf{0}$ for $\ell = 1, \cdots, N$, and the system (49) recovers the hyperelastic model (4).

4 Numerical scheme

The inhomogenous system with source term (49)-(51) is solved numerically by a splitting method. A hyperbolic step solved by a Godunov-type scheme is followed by a relaxation step.

4.1 Hyperbolic step

This Section describes the resolution of the homogeneous part of (49)-(51) without source term. For the sake of simplicity, only 1D projections along x are described; the other projections are treated similarly. Removing ∂_y and ∂_z dependencies, one writes ($\ell = 0, \cdots, N$, $\beta = 1, 2, 3$):

$$
\begin{cases}
\dfrac{\partial \rho}{\partial t} + \dfrac{\partial (\rho u)}{\partial x} = 0, & \text{(54a)} \\
\dfrac{\partial}{\partial t} J_\ell^{-1/2} + \dfrac{\partial}{\partial x}(J_\ell^{-1/2} u) = 0, & \text{(54b)} \\
\dfrac{\partial (\rho u)}{\partial t} + \dfrac{\partial}{\partial x}\left(\rho u^2 - \sigma_{11}\right) = 0, & \text{(54c)} \\
\dfrac{\partial (\rho v)}{\partial t} + \dfrac{\partial}{\partial x}\left(\rho u v - \sigma_{12}\right) = 0, & \text{(54d)} \\
\dfrac{\partial (\rho w)}{\partial t} + \dfrac{\partial}{\partial x}\left(\rho u w - \sigma_{13}\right) = 0, & \text{(54e)} \\
\dfrac{\partial a_\ell^\beta}{\partial t} + \dfrac{\partial}{\partial x}\left(u a_\ell^\beta\right) + b_\ell^\beta \dfrac{\partial v}{\partial x} + c_\ell^\beta \dfrac{\partial w}{\partial x} = 0, & \text{(54f)} \\
\dfrac{\partial b_\ell^\beta}{\partial t} + u \dfrac{\partial b_\ell^\beta}{\partial x} = 0, & \text{(54g)} \\
\dfrac{\partial c_\ell^\beta}{\partial t} + u \dfrac{\partial c_\ell^\beta}{\partial x} = 0. & \text{(54h)}
\end{cases}
$$

This system is nonconservative due to the governing equations of the geometrical variables (54f)-(54h). The resolution of (54) requires to determine the maximal sound velocities. In 3D, the computation of waves speed is very expensive due to the third degree characteristic polynomial, thus we will use an approximate expression of the maximum wave speed:

$$
c^2 = \zeta \sum_{\ell=0}^{N} \left(c_{h\ell}^2 + \frac{4}{3} \frac{\mu_\ell}{\rho_0} \right), \tag{55}
$$

where $c_{h\ell}$ are the hydrodynamic sound velocities (45), and $\zeta \geq 1$ is a security parameter [16, 31]. In the linear case, one recovers the sound speed of longitudinal waves when $\zeta = 1$. The choice of

ζ depends on the studied configuration: $\zeta = 1$ is sufficient for small amplitudes, whereas larger values (typically $\zeta = 5$) may be required for large Mach numbers.

We use the HLLC solver [40], because it preserves the positivity of the density and $J_\ell^{-1/2}$, and is able to deal with strong shock waves. Even if the equations of hyperelasticity contain 7 waves, we will use the solver containing only 3 waves: 2 waves having the most rapid characteristics (they correspond to longitudinal waves), and the contact characteristics. This simple solver is able to capture both longitudinal and transverse waves [19]. With such a solver, each wave is considered as a discontinuity and, consequently, jump relations are needed. The system being nonconservative, the usual Rankine-Hugoniot relation cannot be used, and each jump relation needs to be defined across the waves, as done thereafter.

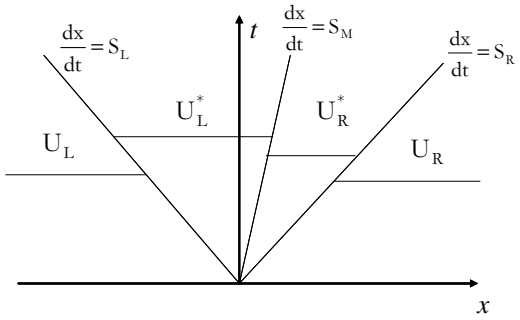

Figure 1: HLLC approximate solver. In the *star* region, two constant states are separated by a wave of speed S_M.

HLLC Riemann solver. We follow the approach proposed in [15, 16, 32]. Let us consider a cell boundary separating a left state (L) and a right state (R), as sketched in Figure 1. The left and right facing wave speeds are obtained following Davis estimates [9]:

$$S_L = \min\left(u_L - c_L, u_R - c_R\right), \qquad S_R = \max\left(u_L + c_L, u_R + c_R\right), \tag{56}$$

where $c_{L,R}$ are the estimated maximal sound speeds (55). The speed of the contact discontinuity is estimated under the HLLC approximation:

$$S_M \equiv u^* = \frac{\left(\rho u^2 - \sigma_{11}\right)_L - \left(\rho u^2 - \sigma_{11}\right)_R - S_L\left(\rho u\right)_L + S_R\left(\rho u\right)_R}{\left(\rho u\right)_L - \left(\rho u\right)_R - \rho_L S_L + \rho_R S_R}. \tag{57}$$

Based on [40, 16], the conservative state variables in the star region are estimated by:

$$\left\{\begin{array}{l}
\rho^*_{L,R} = \rho_{L,R}\dfrac{S_{L,R}-u_{L,R}}{S_{L,R}-u^*},\\
\left(J_\ell^{-1/2}\right)^*_{L,R} = \left(J_\ell^{-1/2}\right)_{L,R}\dfrac{S_{L,R}-u_{L,R}}{S_{L,R}-u^*}, \qquad \ell=0,\cdots,N,\\
\sigma^*_{11} = \dfrac{(u_R-S_R)\,\rho_R\,\sigma_{11L}-(u_L-S_L)\,\rho_L\,\sigma_{11R}+(u_L-S_L)\,\rho_L\,(u_R-S_R)\,\rho_R\,(u_R-u_L)}{(u_R-S_R)\,\rho_R-(u_L-S_L)\,\rho_L},\\
\sigma^*_{12} = \dfrac{(u_R-S_R)\,\rho_R\,\sigma_{12L}-(u_L-S_L)\,\rho_L\,\sigma_{12R}+(u_L-S_L)\,\rho_L\,(u_R-S_R)\,\rho_R\,(v_R-v_L)}{(u_R-S_R)\,\rho_R-(u_L-S_L)\,\rho_L},\\
\sigma^*_{13} = \dfrac{(u_R-S_R)\,\rho_R\,\sigma_{13L}-(u_L-S_L)\,\rho_L\,\sigma_{13R}+(u_L-S_L)\,\rho_L\,(u_R-S_R)\,\rho_R\,(w_R-w_L)}{(u_R-S_R)\,\rho_R-(u_L-S_L)\,\rho_L},\\
v^* = \dfrac{(\rho uv-\sigma_{12})_L-(\rho uv-\sigma_{12})_R-S_L\,(\rho v)_L+S_R\,(\rho v)_R}{(\rho v)_L-(\rho v)_R-\rho_L S_L+\rho_R S_R},\\
w^* = \dfrac{(\rho uw-\sigma_{13})_L-(\rho uw-\sigma_{13})_R-S_L\,(\rho w)_L+S_R\,(\rho w)_R}{(\rho w)_L-(\rho w)_R-\rho_L S_L+\rho_R S_R}.
\end{array}\right. \tag{58}$$

In the case of a fluid-solid interface [32], the velocities v^* and w^* can be discontinuous in the region *star*, so that one must define $v^*_{L,R}$ and $w^*_{L,R}$. In the case of a pure solid considered here, these fields are on the contrary constant in the whole region *star*. Then, the geometric variables are ($\ell=0,\cdots,N$, $\beta=1,2,3$):

$$\left\{\begin{array}{l}
\left(a_\ell^\beta\right)^*_{L,R} = \dfrac{\left(a_\ell^\beta\right)_{L,R}(u_{L,R}-S_{L,R})+\left(b_\ell^\beta\right)_{L,R}(v_{L,R}-v^*)+\left(c_\ell^\beta\right)_{L,R}(w_{L,R}-w^*)}{u^*-S_{L,R}},\\
\left(b_\ell^\beta\right)^*_{L,R} = \left(b_\ell^\beta\right)_{L,R},\\
\left(c_\ell^\beta\right)^*_{L,R} = \left(c_\ell^\beta\right)_{L,R}.
\end{array}\right. \tag{59}$$

With the jump relation presented previously, it is now possible to determine the flux at each cells boundaries. From now on, we will denote with the star superscript * the sampled flux obtained:

$$A^\star = \left\{\begin{array}{lll}
A_L & \text{if} & S_L \geq 0,\\
A_R & \text{if} & S_R \leq 0,\\
A^\star_R & \text{if} & S_M \leq 0 \leq S_R,\\
A^\star_L & \text{if} & S_M \geq 0 \geq S_L.
\end{array}\right. \tag{60}$$

With these definition, we can now derive the numerical scheme.

Godunov scheme. The system (54) contains conservative and nonconservative equations, which are solved successively. The conservative part of (54) reads as a $5+N$ system

$$\frac{\partial \boldsymbol{U}}{\partial t}+\frac{\partial \boldsymbol{f}}{\partial x}=\boldsymbol{0}, \tag{61}$$

with the vector of conserved variables

$$\boldsymbol{U}=\left(\rho,\, J_\ell^{-1/2},\, \rho u,\, \rho v,\, \rho w\right)^\top, \qquad \ell=0,\cdots,N, \tag{62}$$

and the flux

$$\boldsymbol{f}=\left(\rho u,\, J_\ell^{-1/2}u,\, \rho u^2-\sigma_{11},\, \rho uv-\sigma_{12},\, \rho uw-\sigma_{13}\right)^\top. \tag{63}$$

Given a time step Δt and and a mesh size Δx, the usual Godunov scheme is applied [27]:

$$\boldsymbol{U}_i^{n+1} = \boldsymbol{U}_i^n - \frac{\Delta t}{\Delta x}\left(\boldsymbol{f}^*_{i+1/2} - \boldsymbol{f}^*_{i-1/2}\right), \tag{64}$$

where $\boldsymbol{U}_i^n \approx \boldsymbol{U}(x_i = i\Delta x, t_n = t_{n-1} + \Delta t)$. The numerical flux $\boldsymbol{f}^*_{i+1/2} = \boldsymbol{f}^*(\boldsymbol{U}_i^n, \boldsymbol{U}_{i+1}^n)$ is given by the *star* variables: $\boldsymbol{f}^*(\boldsymbol{U}_L, \boldsymbol{U}_R) = \boldsymbol{f}(\boldsymbol{U}^*)$.

The system for the nonconservative part of (54) reads as a $9 \times (N+1)$ system:

$$\frac{\partial \boldsymbol{W}_\ell^\beta}{\partial t} + \frac{\partial \boldsymbol{g}_\ell^\beta}{\partial x} + \boldsymbol{k}_{u,\ell}^\beta \frac{\partial u}{\partial x} + \boldsymbol{k}_{v,\ell}^\beta \frac{\partial v}{\partial x} + \boldsymbol{k}_{w,\ell}^\beta \frac{\partial w}{\partial x} = \boldsymbol{0}, \tag{65}$$

with the vector of nonconserved variables

$$\boldsymbol{W}_\ell^\beta = \left(a_\ell^\beta,\, b_\ell^\beta,\, c_\ell^\beta\right)^\top, \qquad \ell = 0, \cdots, N, \qquad \beta = 1, 2, 3, \tag{66}$$

and the fluxes

$$\boldsymbol{g}_\ell^\beta = \left(ua_\ell^\beta,\, ub_\ell^\beta,\, uc_\ell^\beta\right)^\top, \quad \boldsymbol{k}_{u,\ell}^\beta = \left(0,\, -b_\ell^\beta,\, -c_\ell^\beta\right)^\top, \quad \boldsymbol{k}_{v,\ell}^\beta = \left(b_\ell^\beta,\, 0,\, 0\right)^\top, \quad \boldsymbol{k}_{w,\ell}^\beta = \left(c_\ell^\beta,\, 0,\, 0\right)^\top. \tag{67}$$

The nonconservative equations (65) are solved by the scheme:

$$\begin{aligned}\left(\boldsymbol{W}_\ell^\beta\right)_i^{n+1} = \left(\boldsymbol{W}_\ell^\beta\right)_i^n - \frac{\Delta t}{\Delta x}\Big[&\left(\boldsymbol{g}_\ell^\beta\right)^*_{i+1/2} - \left(\boldsymbol{g}_\ell^\beta\right)^*_{i-1/2} \\ &+ \left(\boldsymbol{k}_{u,\ell}^\beta\right)_i^n \left(u^*_{i+1/2} - u^*_{i-1/2}\right) \left(\boldsymbol{k}_{v,\ell}^\beta\right)_i^n \left(v^*_{i+1/2} - v^*_{i-1/2}\right) + \left(\boldsymbol{k}_{w,\ell}^\beta\right)_i^n \left(w^*_{i+1/2} - w^*_{i-1/2}\right)\Big].\end{aligned} \tag{68}$$

The numerical flux $\left(\boldsymbol{g}_\ell^\beta\right)^*_{i+1/2} = \left(\boldsymbol{g}_\ell^\beta\right)^* \left(\left(\boldsymbol{W}_\ell^\beta\right)_i^n, \left(\boldsymbol{W}_\ell^\beta\right)_{i+1}^n\right)$ is given by the *star* variables: $\left(\boldsymbol{g}_\ell^\beta\right)^* (\boldsymbol{W}_L, \boldsymbol{W}_R) = \boldsymbol{g}_\ell^\beta(\boldsymbol{W}^*)$. In (68), $u^*_{i\pm1/2}$ are the normal velocity components at the cell boundaries, $v^*_{i-1/2}$ and $w^*_{i+1/2}$ are the corresponding tangential velocity components.

The conservative and nonconservative parts of the Godunov scheme are solved simultaneously. As already pointed out, only 1D fluxes are written (64) and (68). For multidimensional problems, these fluxes must be completed by the y and z dependencies. The CFL condition of stability of this method is

$$\mathrm{CFL} = \max(c)\frac{\Delta t}{\Delta x} \leq \gamma \tag{69}$$

where $\max(c)$ denotes the maximal value of (55) over the computational domain, and γ depends on the space dimension [27]. In 1D, $\gamma = 1$, whereas $\gamma = 0.5$ in higher space dimensions.

4.2 Relaxation step

In the system (49)-(51), the only equations that are changing during the relaxation step are

$$\begin{cases} \dfrac{\partial \boldsymbol{e}_\ell^\beta}{\partial t} = \dfrac{\theta_\ell}{2\mu_\ell}\left(\boldsymbol{\sigma}_\ell - \dfrac{\lambda_\ell}{3\lambda_\ell + 2\mu_\ell}\,\mathrm{tr}\boldsymbol{\sigma}_\ell\, \boldsymbol{I}\right).\boldsymbol{e}_\ell^\beta, \qquad \ell = 1, \cdots, N, \qquad \beta = 1, 2, 3, & \text{(70a)} \\ \dfrac{\partial}{\partial t} J_\ell^{-1/2} = \dfrac{\theta_\ell}{3\lambda_\ell + 2\mu_\ell}\,\mathrm{tr}\boldsymbol{\sigma}_\ell\, J_\ell^{-1/2}, \qquad \ell = 1, \cdots, N. & \text{(70b)} \end{cases}$$

This system of $10 \times N$ ordinary differential equations could be solved by any numerical integrator. However, a naive resolution of (70) would not ensure $|\boldsymbol{F}_\ell| > 0$, which is essential when computing the energy (37).

An alternative approach is followed here to ensure the positivity of $|\boldsymbol{F}_\ell|$ and J_ℓ. Assuming that $\boldsymbol{\sigma}_\ell$ is constant during the relaxation step, then (70) can be integrated exactly:

$$\left\{ \begin{array}{ll} \left(\boldsymbol{e}_\ell^\beta\right)^{n+1} = \exp\left(\dfrac{\theta_\ell \Delta t}{2\mu_\ell}\left(\boldsymbol{\sigma}_\ell - \dfrac{\lambda_\ell}{3\lambda_\ell + 2\mu_\ell}\,\mathrm{tr}\boldsymbol{\sigma}_\ell\, \boldsymbol{I}\right)\right) . \left(\boldsymbol{e}_\ell^\beta\right)^{n}, & \ell = 1, \cdots, N,\ \beta = 1,2,3, \quad (71a) \\ \left(J_\ell^{-1/2}\right)^{n+1} = \exp\left(\dfrac{\theta_\ell \Delta t}{3\lambda_\ell + 2\mu_\ell}\,\mathrm{tr}\boldsymbol{\sigma}_\ell\right)\left(J_\ell^{-1/2}\right)^{n}, & \ell = 1, \cdots, N. \quad (71b) \end{array} \right.$$

The computation of the matrix exponential (71a) is done by a (6, 6) Padé approximation of the "scaling and squaring method" [30]. The equation on $J_\ell^{-1/2}$ is used only in the hydrodynamic pressure (39). Doing so provides an easy mean to guarantee that isochoric transformations do not modify the hydrodynamic energy (38), as proven in Appendix A.

5 Numerical examples

5.1 Shear Riemann problem

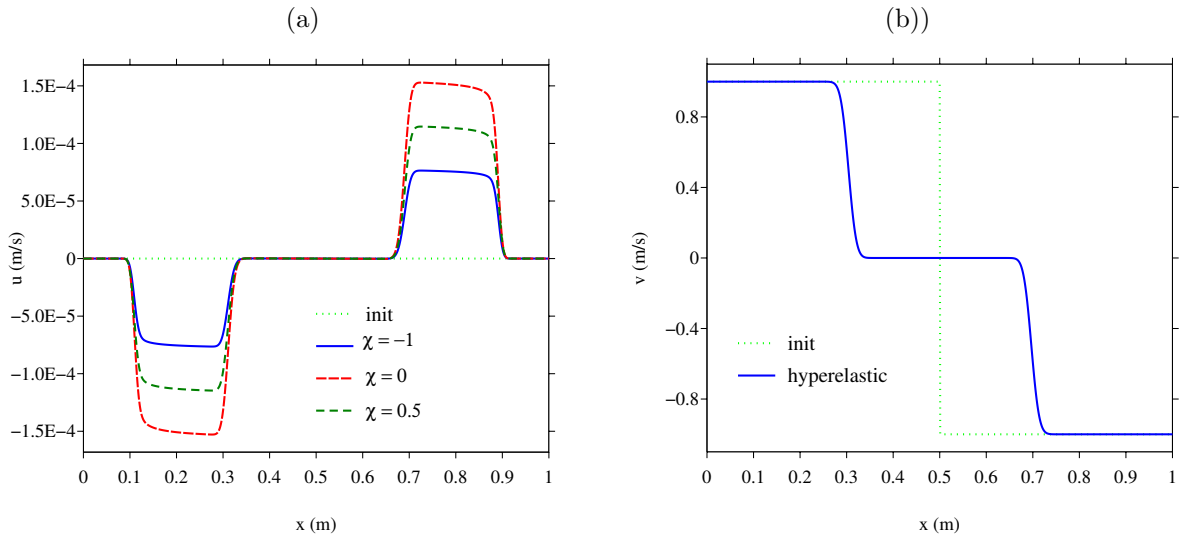

Figure 2: Shear Riemann problem in hyperelasticity at $t = 1.4 \times 10^{-4}$ s. Initially a discontinuous tangential velocity is imposed (dashed line). Various values of the nonlinear parameter χ are considered.

A domain $[0, 1]$ of length $L = 1$ m is discretized on 1000 grid points. The medium is hyperelastic, with reference density $\rho_0 = 1200$ kg.m^{-3}, compressional wave velocity $c_p(0) = 2800$ m/s, and shear wave velocity $c_s(0) = 1400$ m/s. These parameters are representative of media such as Plexiglass [28]. The fields are initially zero, except the tangential velocity which is discontinuous at $t = 0$ and $x_0 = 0.5$ m: $v = +1$ m/s for $x < x_0$, and $v = -1$ m/s for $x > x_0$. At $t > 0$, the velocity and the normal stress are continuous along x_0. The maximum wave speed is computed using $\zeta = 1.2$ (55), and the CFL number is 0.95 (69). The computations are done with double accuracy (8 octets per real number). This coding is sufficient to discretize small variations of ρ.

Figure 2 represents the longitudinal and tangential velocities at $t = 1.4 \times 10^{-4}$ s. In linear regime, u would remain identically zero. On the contrary, one observes here that longitudinal

waves are generated, which is the signature of a nonlinear coupling. The amplitude of these longitudinal waves depends on the nonlinear parameter $\chi_0 \equiv \chi$. The tangential component of the velocity v has right-going and left-going shock waves, and is independent of χ for the amplitude considered here. From now on, we will consider $\chi_\ell = 0$. Finally, we note that u (a) has two fronts: the leading front corresponds to compressional waves, while the trailing front corresponds to shear waves. For v (b), there are logically only discontinuities associated with shear waves.

5.2 Impact Riemann problem

	θ_ℓ (s^{-1})	κ_ℓ	θ_ℓ (s^{-1})	κ_ℓ
$\ell = 1$	1652	0.386	1372	0.0874
$\ell = 2$	14153	0.399	11885	0.0723
$\ell = 3$	123603	0.726	103368	0.1025

Table 1: Optimized parameters of viscoelasticity for the impact Riemann problem. The range of optimization is $[1.12 \times 10^3, 1.12 \times 10^5]$ Hz. Left part: $Q = 5$; right part: $Q = 20$.

Given the same parameters as before, we now consider an impact with a longitudinal velocity discontinuity: $u = +1$ m/s for $x < x_0$, and $u = -1$ m/s for $x > x_0$. The dissipation is accounted for by $N = 3$ relaxation mechanisms, with the same quality factor for compressional and longitudinal waves: $Q_p = Q_s \equiv Q$. The value $Q = 20$ corresponds to low dissipation, while $Q = 5$ corresponds to high dissipation. The parameters of the GZM are optimised over a frequency band $[f_{\min}, f_{\max}]$, with $f_{\min} = f_c/10$ and $f_{\max} = 10 \times f_c$ [4]. The central frequency is chosen so that $f_c = c_p/\Lambda$, where Λ is a characteristic wavelength. Here $\Lambda = L/4 = 0.25$ m is chosen, so that $f_c = 11.2$ kHz. The optimized parameters are given in Table 1.

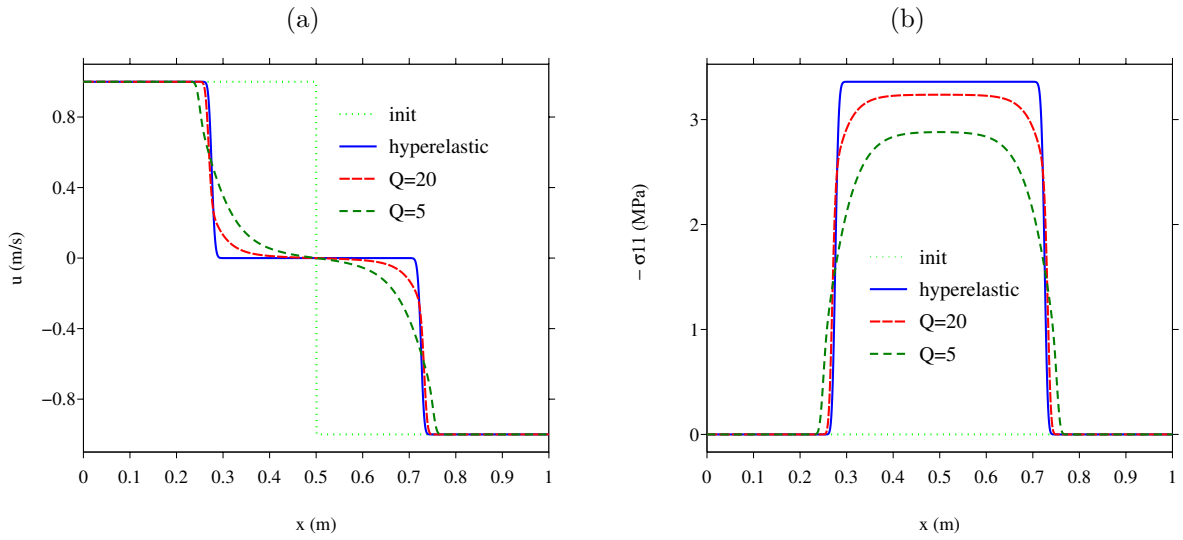

Figure 3: Impact Riemann problem at $t = 8 \times 10^{-5}$ s. Initially a discontinuous longitudinal velocity is imposed (dashed line). Various values of attenuation are considered: null (hyperelasticity), weak ($Q = 20$) and large ($Q = 5$). Left: u; right: $-\sigma_{11}$.

Figure 3 shows the longitudinal velocity u and the total stress component $-\sigma_{11}$ (in MPa) at $t = 8 \times 10^{-5}$ s. In the absence of dissipation (hyperelastic medium), shock waves propagate in both directions. As the attenuation increases, the sharp fronts are smoother, and the amplitude of $-\sigma_{11}$ decreases.

5.3 Compressive source point in 1D

We consider a 1D problem with a source point at $x_s = 0.5$ m, which emits a compressive sine wave from $t = 0$. In (49b), the source term is then $\boldsymbol{s}(x,t) = A \sin(\omega_c t)\, H(t)\, \delta(x - x_s)\, (1,0,0)^\top$ with the amplitude $A = 4 \times 10^9$ Pa/m, the angular frequency $\omega_c = 2\pi\, f_c$, and δ the Dirac delta function. The central frequency is $f_c = 20$ kHz. The quality factor is $Q = 5$; the parameters of the GZM ($N = 3$ relaxation mechanisms) are optimised accordingly. The optimized parameters are given in the left part of Table 2.

	θ_ℓ (s^{-1})	κ_ℓ	θ_ℓ (s^{-1})	κ_ℓ
$\ell = 1$	2950	0.386	1475	0.386
$\ell = 2$	25271	0.399	12637	0.399
$\ell = 3$	220716	0.726	110359	0.726

Table 2: Optimized parameters of viscoelasticity for the source point problems. The quality factor is $Q = 5$. Left part: 1D case, with optimization range $[2 \times 10^3,\, 2 \times 10^5]$ Hz. Right part: 2D case, with optimization range $[10^3,\, 10^5]$ Hz.

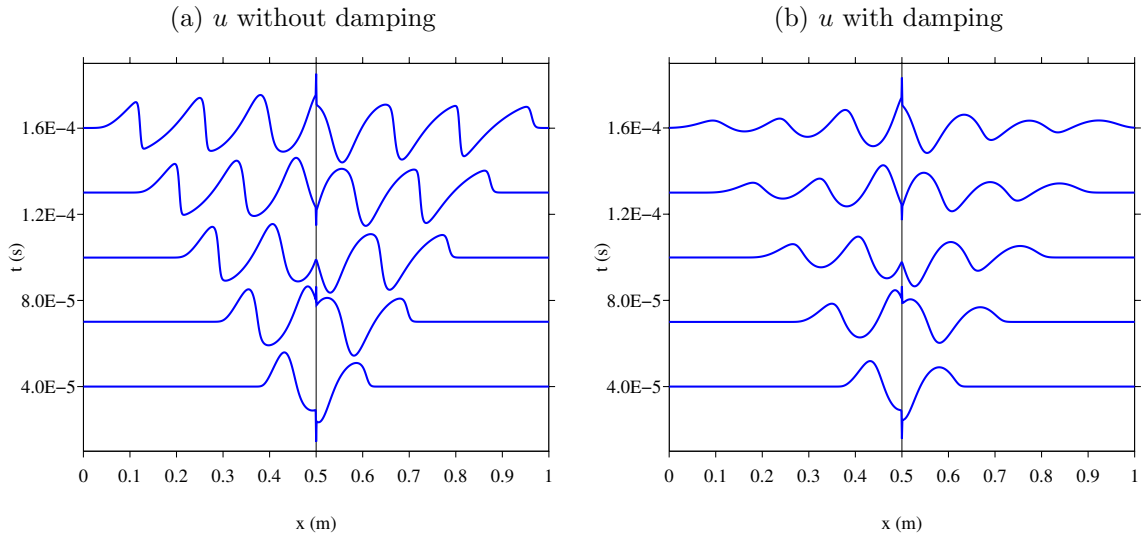

Figure 4: Compressive source point in 1D. Seismogram of u. A monochromatic source at $x_s = 0.5$ (denoted by a vertical line) emits compressive waves with an amplitude $A = 4 \times 10^9$ Pa/m and a central frequency $f_c = 20$ kHz. (a): hyperelastic medium. (b): viscoelastic medium, with $Q = 5$ ($N = 3$ relaxation mechanisms).

Figure 4 displays seismograms of u at $t = (4 + 3(i-1))\, 10^{-5}$ s, $i = 1, \cdots, 4$. In the hyperelastic case (a), we observe the asymmetry of u with respect to the source point. Another signature of

nonlinearities is the sharpening of fronts. In the case of the GZM (b), u is still asymmetric. However, the dissipation is sufficient to smooth the sharp fronts and to prevent the occurrence of shocks.

5.4 Shear source point in 1D

We consider a 1D problem with a point source at $x_s = 0.5$ m, which emits a shear sine wave from $t = 0$. In (49b), the source term is then $\boldsymbol{s}(x,t) = A\sin(\omega_c t)\, H(t)\, \delta(x - x_s)\, (0,1,0)^\top$. All the parameters are the same as in the previous test with the compressive source. In particular, the amplitude of the forcing is $A = 4 \times 10^9$ Pa/m, and the central frequency is $f_c = 20$ kHz.

Figure 5 displays seismograms of u and v each 3 ms. In linear regime, no compressional wave would be emitted, as recalled in Section 5.1. On the contrary, one observes clearly in (a-c) a u component. The latter shear wave propagates slower. For both components, the effect of viscoelasticity is clearly seen through the damping of waves.

5.5 Source point in 2D

As a last example, we consider a 2D domain $[-0.5, 0.5]^2$, discretized on 300×300 points in space. The parameters of the viscoelastic medium are the same as before, with $Q_p = Q_s = 5$. The optimized parameters are given in the right part of Table 2. A source is placed in the center of the domain. The forcing (49b) is $\boldsymbol{s}(\boldsymbol{x},t) = A\, r(\boldsymbol{x})\, g(t)\, (1,0,0)^\top$. The spatial distribution r is a truncated Gaussian distribution of truncation radius $r_0 = 0.08$ m and standard deviation $\Sigma_0 = 0.04$ m:

$$r(x,y) = \begin{cases} \dfrac{1}{\pi\,\Sigma_0^2} \exp\left(-\dfrac{x^2+y^2}{\Sigma_0^2}\right) & \text{if } 0 \leqslant x^2+y^2 \leqslant r_0^2, \\ 0 & \text{otherwise.} \end{cases} \tag{72}$$

By regularising the Dirac in this way, singularities in the solution (due to the 2D space dimension) and spurious oscillations at the source are avoided. The time evolution $g(t)$ is a Ricker wavelet of central frequency $f_c = 10$ kHz and of time shift $t_c = 2/f_c = 0.2$ s:

$$g(t) = \begin{cases} \left(2\,\pi^2\, f_c^2 \left(t - \dfrac{1}{f_c}\right)^2 - 1\right) \exp\left(-\pi^2\, f_c^2 \left(t - \dfrac{1}{f_c}\right)^2\right) & \text{if } 0 \leqslant t \leqslant t_c, \\ 0 & \text{otherwise.} \end{cases} \tag{73}$$

Two forcing amplitudes are considered: $A = 10^7$ Pa/m (low amplitude) and $A = 10^9$ Pa/m (large amplitude). A receiver in $(x_r = 0.05, y_r = 0.05)$ records the field at each iteration. It is denoted by a yellow cross on the maps of Figure 6.

The maps in Figure 6 show u and v at $t = 1.9 \times 10^{-4}$ s. At low amplitude (a-b), we observe the expected properties of symmetry of u with respect to $x = 0$, and of central symmetry of v. We also observe on v the separation into compressional and shear waves. At high amplitudes (c-d), the symmetry properties are lost, which is a signature of nonlinear effects.

Sub-figure 6-(e,f) shows the time evolution of u and v measured at the receiver, up to $t = 3 \times 10^{-4}$ s. Each field is normalized by its maximum absolute value. The normalized signals obtained with the linear GZM [28] and with the nonlinear model are superimposed. At low amplitude ($A = 10^7$ Pa/m), we note the good agreement between the linear model and the nonlinear GZM: the nonlinear effects are moderate. At large amplitude ($A = 10^9$ Pa/m), the nonlinear effects distort the signals significantly.

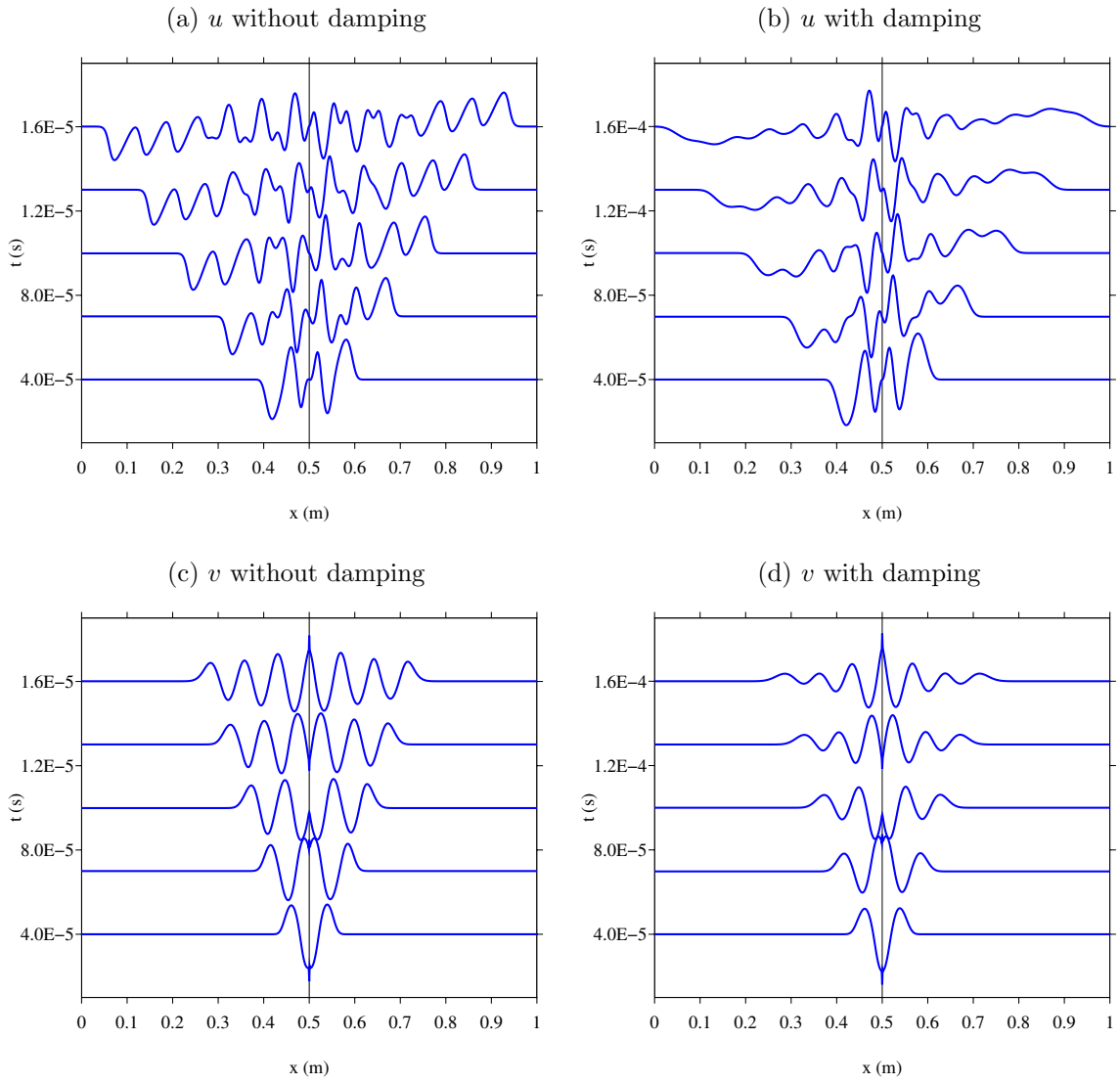

Figure 5: Shear source point in 1D. Seismogram of u (left row) and v (right row) at $t = (4 + 3(i-1))\,10^{-5}$ s, $i = 1, \cdots, 4$. A monochromatic source at $x_s = 0.5$ (denoted by a vertical line) emits shear waves with an amplitude $A = 2 \times 10^7$ Pa/m and a central frequency $f_c = 20$ kHz. Left (a-c): hyperelastic medium. Right (b-d): viscoelastic medium, with $Q = 5$ ($N = 3$ relaxation mechanisms).

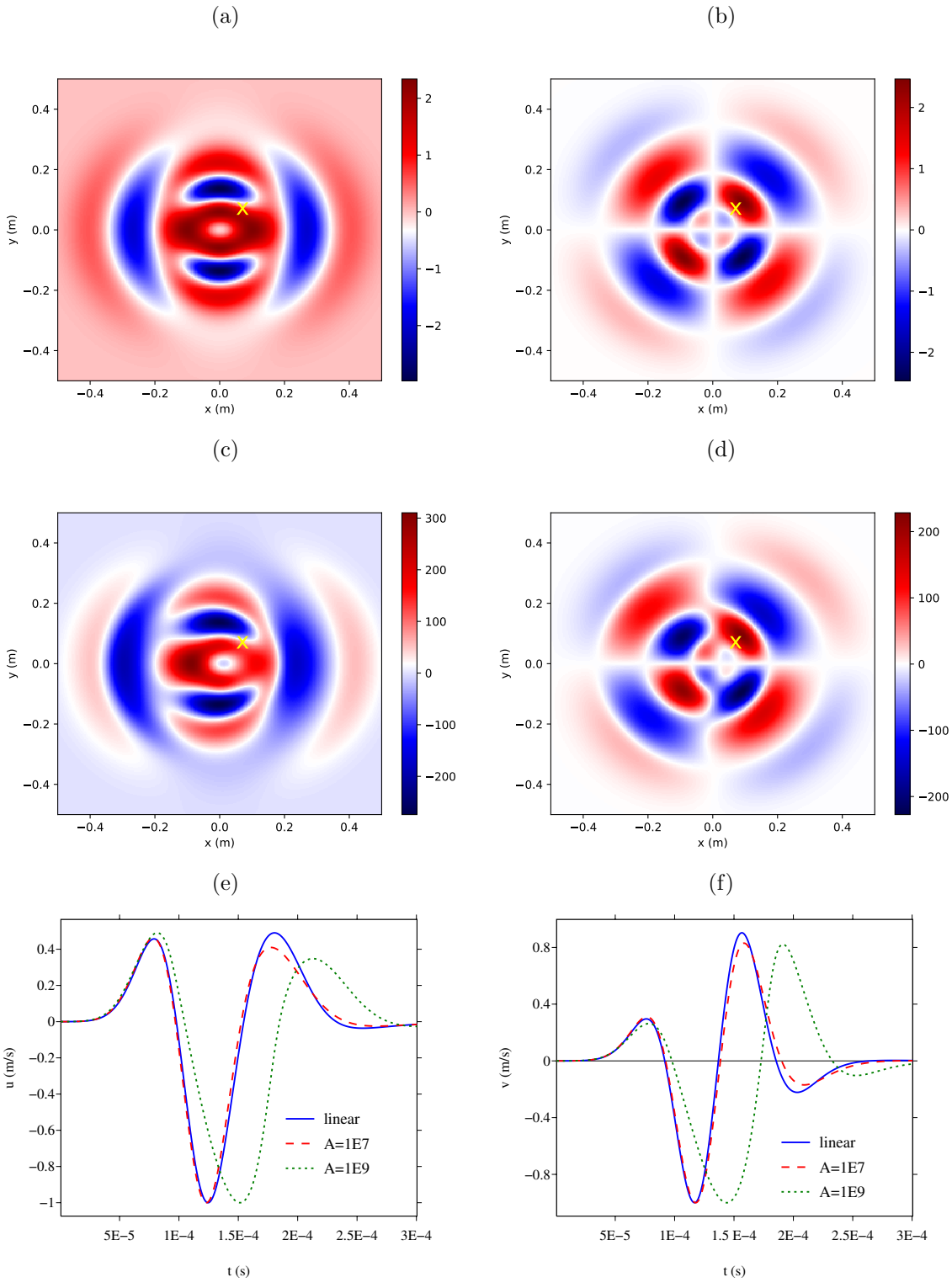

Figure 6: Two dimensional fields emitted by a source point at $t = 1.9 \times 10^{-4}$ s at absissa (0,0). The yellow $\times$ symbol denotes the receiver. The maps represent u (left) and v, for low amplitudes (a-b) and large amplitudes (c-d). The curves display the time evolution of the normalized u (e) and v (f) computed by the linear GZM and by the nonlinear GZM, for two amplitudes of forcing A.

6 Conclusion

We have proposed a nonlinear viscoelastic model well adapted to the dynamic regime. This model degenerates towards two classical limit cases: (i) hypelasticity when dissipation cancels; (ii) the linear GZM in small deformations. This model is dissipative and unconditionally hyperbolic, leading to explicit and reliable numerical schemes. A Godunov numerical scheme has been implemented in the PROSPERO software [1] to illustrate the phenomenology of nonlinear viscoelastic waves, showing coupling between compressional and shear waves, effect of dissipation on the wave fronts, and non-reciprocity of the wave fields.

This work constitutes a step towards the modelling of large amplitude waves in biological tissues. The theoretical and numerical model developed here could thus make a contribution to the simulation of shock waves in the brain, during a cranial trauma [13]. A similar approach can also be followed to describe a richer phenomenology. One thinks in particular of thermo-elastic solids, or of the study of waves in yield stresses fluids [34].

A limitation of this study concerns the constitutive assumptions. The choice of the EOS in separable form (32) with hydrodynamic energy (38) and shear energy (46) ensures hyperbolicity but is restrictive. Other constitutive laws (such as the classical Mooney-Rivlin model of hyperelasticity) can be used in the framework treated here, but without warranty of hyperbolicity. Conversely, very few theoretical results are known for the EOS we use here, which raises further investigation. One thinks in particular to the computation of the solution of the Riemann problem and to the existence of kink waves [11].

Another direction for further works concerns the numerical scheme. The first-order numerical scheme used is robust and works even for very large strains, but it introduces numerical diffusion. The implementation of more sophisticated schemes should lead to significant improvements, for example finite-volume schemes with flux limiters [27] or ADER schemes [6]. One of the difficulties lies in the discretisation of the nonconservative terms (65).

Acknowledgement. The authors thank to Stéphane Lejeunes (LMA, Marseille) for stimulating discussions. N.F. acknowledges support from the ANR under grant ANR-ASTRID project SNIP ANR-19-ASTR-0016-01. This work was done in the framework of the Institut de Mécanique de Marseille (France). Finally, the authors greatly thank the Reviewers for their constructive comments, which helped to substantially improve the manuscript.

A Utility of an evolution equation for J_ℓ

Equation (51a) gives $\boldsymbol{C}_\ell^{-1} = \boldsymbol{F}_\ell^{-1}.\boldsymbol{F}_\ell^{-\top}$. Numerical estimation of $\boldsymbol{F}_\ell^{-\top}$ thus allows to compute $J_\ell = |\boldsymbol{C}_\ell|$ used in the hydrodynamic equations (38) and (39). However, a difficulty arises when considering a isochoric transformation. Hydrodynamic energy (38) and pressure (39) are constant at the continuous level, but may change at the discrete level. The goal of this Appendix is to highlight this inconsistency through an example, and then to show that an additional evolution equation for J_ℓ fixes the problem.

Let a hyperelastic medium undergo the 2D isochoric transformation:

$$\left\{\begin{array}{l} x = X\ \exp(+\omega\, t), \\ y = Y\ \exp(-\omega\, t), \end{array}\right. \tag{74}$$

with ω constant (in s^{-1}), hence $u = +\omega\, x$ and $v = -\omega\, y$. Since $\mathrm{div}\boldsymbol{v} = 0$, then (10) ensures that J is constant, and it is obviously the same for $J^{-1/2}$ (in hyperelasticity no index ℓ is required, and no source term occurs). Let us now turn to the discrete equations, with $\Delta x = \Delta y$. The transformation (74) leads to

$$\left(\boldsymbol{F}^{-T}\right)_{i,j}^{n} = \begin{pmatrix} \left(a^1\right)_{i,j}^{n} & \left(a^2\right)_{i,j}^{n} \\ \left(b^1\right)_{i,j}^{n} & \left(b^2\right)_{i,j}^{n} \end{pmatrix} \equiv \begin{pmatrix} \left(a^1\right)_{i,j}^{n} & 0 \\ 0 & \left(b^2\right)_{i,j}^{n} \end{pmatrix}. \tag{75}$$

The discretization of the cobasis equations (51a) writes:

$$\begin{aligned} \left(a^1\right)_{i,j}^{n+1} &= \left(a^1\right)_{i,j}^{n} - \left(a^1\right)_{i,j}^{n} \frac{\Delta t}{\Delta x}\left(u_{i+1/2,j}^{n} - u_{i-1/2,j}^{n}\right), \\ \left(b^2\right)_{i,j}^{n+1} &= \left(b^2\right)_{i,j}^{n} - \left(b^2\right)_{i,j}^{n} \frac{\Delta t}{\Delta x}\left(v_{i,j+1/2}^{n} - v_{i,j-1/2}^{n}\right). \end{aligned} \tag{76}$$

Let us assume that the scheme satisfies $\mathrm{div}\boldsymbol{v} = 0$ at the discrete level. From (51b), it follows that $\left(J^{-1/2}\right)_{i,j}$ is conserved:

$$\begin{aligned} \left(J^{-1/2}\right)_{i,j}^{n+1} - \left(J^{-1/2}\right)_{i,j}^{n} &= -\left(J^{-1/2}\right)_{i,j}^{n} \frac{\Delta t}{\Delta x}\left(u_{i+1/2,j}^{n} - u_{i-1/2,j}^{n} + v_{i,j+1/2}^{n} - v_{i,j-1/2}^{n}\right), \\ &= 0. \end{aligned} \tag{77}$$

On the other hand, from (75) and (76) one obtains

$$\begin{aligned} \left(J^{-1/2}\right)_{i,j}^{n+1} &= \left|\left(\boldsymbol{F}^{-T}\right)_{i,j}^{n+1}\right|, \\ &= \left(a^1\right)_{i,j}^{n+1}\left(b^2\right)_{i,j}^{n+1}, \\ &= \left(a^1\right)_{i,j}^{n}\left(b^2\right)_{i,j}^{n} \times \left[1 - \frac{\Delta t}{\Delta x}\left(u_{i+1/2,j}^{n} - u_{i-1/2,j}^{+} v_{i,j+1/2}^{n} - v_{i,j-1/2}^{n}\right)\right. \\ &\qquad \left. + \left(\frac{\Delta t}{\Delta x}\right)^2 \left(u_{i+1/2,j}^{n} - u_{i-1/2,j}^{n}\right)\left(v_{i,j+1/2}^{n} - v_{i,j-1/2}^{n}\right)\right], \\ &= \left(J^{-1/2}\right)_{i,j}^{n}\left[1 - \left(\frac{\Delta t}{\Delta x}\right)^2 \left(u_{i+1/2,j}^{n} - u_{i-1/2,j}^{n}\right)\left(v_{i,j+1/2}^{n} - v_{i,j-1/2}^{n}\right)\right]. \end{aligned} \tag{78}$$

The isochoric transformation thus leads to a nonphysical variation of $\left(J^{-1/2}\right)_{i,j}^{n+1}$ of order $(\Delta t/\Delta x)^2 \approx (\mathrm{CFL}/c)^2$. The resolution of (51b) fixes this problem in a simple and efficient way.

References

[1] C. Bellis, B. Lombard, *Simulating transient wave phenomena in acoustic metamaterials using auxiliary fields*, Wave Motion, 86 (2019), 175-194.

[2] H. Berjamin, N. Favrie, B. Lombard, G. Chiavassa, *Nonlinear waves in solids with slow dynamics: an internal-variable model*, Proceedings Royal Society London A 473 (2017), 20170024.

[3] H. Berjamin, S. Chockalingam, *Shear shock formation in incompressible viscoelastic solids*, Wave Motion, 110 (2022), 102899.

[4] E. Blanc, D. Komatitsch, E. Chaljub, B. Lombard, Z. Xie, *Highly-accurate stability-preserving optimization of the Zener viscoelastic model, with application to wave propagation in the presence of attenuation*, Geophysical Journal International, 205 (2016), 427-439.

[5] S. Chockalingam, T. Cohen, *Shear shock evolution in incompressible soft solids*, Journal of the Mechanics and Physics of Solids, 134 (2020), 103746.

[6] S. Busto Ulloa, S. Chiocchetti, M. Dumbser, E. Gaburro, I. Peshkov, *High Order ADER Schemes for Continuum Mechanics*, Frontiers in Physics, 8 (2020).

[7] J.M. Carcione, *Wave Fields in Real Media: Wave Propagation in Anisotropic, Anelastic, Porous and Electromagnetic Media*, Pergamon (2007).

[8] J. D. Clayton, A. D. Freed, *A constitutive model for lung mechanics and injury applicable to static, dynamic, and shock loading*, Mechanics of Soft Materials, 2-3 (2020).

[9] S.F. Davis, *Simplified second-order Godunov-type methods*, SIAM J. Sci. Stat. Comput., 9 (1988), 445-473.

[10] R. De Pascalis, D. Abrahams, W. J. Parnell, *On nonlinear viscoelastic deformations: a reappraisal of Fung's quasilinear viscoelastic model*, Proceedings Royal Society London A 470 (2014), 20140058.

[11] R. De Pascalis, G. Napoli, G. Saccomandi, *Kink-type solitary waves within the quasi-linear viscoelastic model*, Wave Motion, 86 (2019), 195–202.

[12] N. Delépine, L. Lenti, G. Bonnet, J.F. Semblat, *Non-linear viscoelastic wave propagation: an extension of nearly constant attenuation models*, Journal of Engineering Mechanics, 135-11 (2009), 1305–1314.

[13] D. Espíndola, S. Lee, G. Pinton, *Shear shock waves observed in the brain*, Physical Review Applied, 8-4 (2017), 044024.

[14] N. Favrie, S. Gavrilyuk, *Mathematical and numerical model for nonlinear viscoplasticity*, Philosophical Transactions of the Royal Society of London A: Mathematical, Physical and Engineering Sciences, 369 (2011), 2864-2880.

[15] N. Favrie, S. Gavrilyuk, *Diffuse interface model for compressible fluid – Compressible elastic–plastic solid interaction*. Journal of Computational Physics, 231 (2012), 2695-2723.

[16] N. Favrie, S. Gavrilyuk, S. Ndanou, *A thermodynamically compatible splitting procedure in hyperelasticity*, Journal of Computational Physics, 270 (2014), 300-324.

[17] N. Favrie, B. Lombard, C. Payan, *Fast and slow dynamics in a nonlinear elastic bar excited by longitudinal vibrations*, Wave Motion, 56 (2015), 221-238.

[18] Y. C. Fung, *Biomechanics: Mechanical Properties of Living Tissues*, Springer-Verlag, New York (1981).

[19] S. Gavrilyuk, N. Favrie, R. Saurel, *Modelling wave dynamics of compressible elastic materials*, Journal of Computational Physics, 227 (2008), 2941–2969.

[20] S. Gavrilyuk, S. Ndanou, S. Hank, *An example of a one-parameter family of rank-one convex stored energies for isotropic compressible solids*, Journal of Elasticity, 124 (2016), 133-141.

[21] S.K. Godunov, E.I. Romenskii, *Elements of Continuum Mechanics and Conservation Laws*, Kluwer Academic Plenum Publishers, NY (2003).

[22] G. A. Holzapfel, *Nonlinear Solid Mechanics: A Continuum Approach for Engineering*, John Wiley & Sons Ltd., 2000.

[23] A.G. Kulikovskii, E.I. Sveshnikova, *Nonlinear Waves in Elastic Media*, CRC Press, 2021.

[24] A. Kumar, O. Lopez-Pamies, *On the two-potential constitutive modeling of rubber viscoelastic materials*, Comptes Rendus Mécanique, 344-2(2016), 102-112.

[25] P. Le Tallec, C. Rahier, A. Kaiss, *Three-dimensional incompressible viscoelasticity in large strains: formulation and numerical approximation*, Computer Methods in Applied Mechanics and Engineering, 109 (1993), 233-258.

[26] J. Lemaitre, J.-L. Chaboche, A. Benallal, R. Desmorat, *Mécanique des Matériaux Solides*, 3rd Edition, Dunod, 2009.

[27] R.J. LeVeque, *Finite Volume Methods for Hyperbolic Problems*, Cambridge University Press (2002).

[28] B. Lombard, J. Piraux, *Numerical modeling of transient two-dimensional viscoelastic waves*, Journal of Computational Physics, 230 (2011), 6099-6114.

[29] R. Martin, L. Bodet, V. Tournat, F. Reijiba, *Seismic wave propagation in nonlinear viscoelastic media using the auxiliary differential equation method*, Geophysical Journal International, 216 (2019), 453-469.

[30] C.B. Moller, C.F. Loan, *Nineteen dubious ways to compute the exponential of a matrix, twenty-five years later*, SIAM Review, 45 (2003), 3–49.

[31] S. Ndanou, N. Favrie, S. Gavrilyuk, *Criterion of hyperbolicity in hyperelasticity in the case of the stored energy in separable form*, Journal of Elasticity, 115 (2014), 1-25.

[32] S. Ndanou, N. Favrie, S. Gavrilyuk, *Multi-solid and multi-fluid diffuse interface model: applications to dynamic fracture and fragmentation*, Journal of Computational Physics, 295 (2015), 523-555.

[33] S. Ndanou, N. Favrie, S. Gavrilyuk, *The piston problem in hyperelasticity with the stored energy in separable form*, Mathematics and Mechanics of Solids, 22-1, (2017), 101-113.

[34] A. Perelomova, *Propagation of acoustic pulses in some fluids with yield stress*, Canadian Journal of Physics, 89 (2011), 219-224.

[35] S. Reese, S. Govindjee, *A theory of finite viscoelasticity and numerical aspects*, International Journal of Solids and Structures, 35 (1998), 3455-3482.

[36] J.O.A. Robertsson, J.O. Blanch, W.W. Symes, *Viscoelastic finite-difference modeling*, Geophysics, 59-9 (1994), 1444-1456.

[37] K. W. Schuler, J. W. Nunziato, E. K. Walsh, *Recent results in nonlinear viscoelastic wave propagation*, International Journal of Solids and Structures, 9 (1973), 1231-1281.

[38] J. Simo, *On a fully three-dimensional finite-strain viscoelastic damage model: formulation and computational aspects*, Computer Methods in Applied Mechanics and Engineering, 60-2 (1987), 153–173.

[39] B.B. Tripathi, D. Espíndola, G.F. Pinton, *Modeling and simulations of two dimensional propagation of shear shock waves in relaxing soft solids*, Journal of Computational Physics 395 (2019), 205-222.

[40] E. F. Toro, *Riemann Solvers and Numerical Methods for Fluid Dynamics. A Practical Introduction*, Springer-Verlag (1999).

[41] V. Tournat, V. Gusev, *Acoustics of unconsolidated model granular media: an overview of recent results and several open problems*, Acta Acustica United Acustica, 96 (2010), 208–224.

[42] A. Wineman, *Nonlinear viscoelastic solids—a review*, Mathematics and Mechanics of Solids, 14-3 (2009), 300–366.